

LA-UR-18-30520

Approved for public release; distribution is unlimited.

Title: PUMA: Plutonium Modeling and Analysis Theory Manual Rev 1.0

Author(s): Matthews, Christopher
Cooper, Michael William Donald

Intended for: Report

Issued: 2018-11-02

Disclaimer:

Los Alamos National Laboratory, an affirmative action/equal opportunity employer, is operated by the Los Alamos National Security, LLC for the National Nuclear Security Administration of the U.S. Department of Energy under contract DE-AC52-06NA25396. By approving this article, the publisher recognizes that the U.S. Government retains nonexclusive, royalty-free license to publish or reproduce the published form of this contribution, or to allow others to do so, for U.S. Government purposes. Los Alamos National Laboratory requests that the publisher identify this article as work performed under the auspices of the U.S. Department of Energy. Los Alamos National Laboratory strongly supports academic freedom and a researcher's right to publish; as an institution, however, the Laboratory does not endorse the viewpoint of a publication or guarantee its technical correctness.



PUMA: Plutonium Modeling and Analysis

Theory Manual

Rev 1.0

Christopher Matthews

Michael Cooper

LOS ALAMOS NATIONAL LABORATORY

September 2018

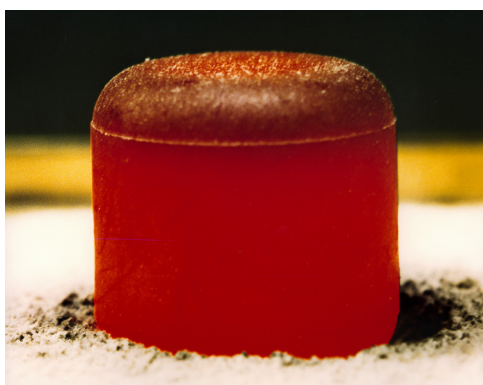
Contents

1	Introduction	1
2	PUMA Code Description	3
2.1	MOOSE	3
2.2	PUMA objects	3
2.2.1	Materials	4
2.2.2	AuxKernels	16
2.2.3	Functions	17
2.3	Meshing	18
2.4	Boundary Conditions	18
2.5	Run Settings	20
3	Results	21
3.1	Plutonia baseline	21
3.2	Ceria baseline	27
3.3	Mesh and Geometry changes	29
3.4	Parametric studies	30
4	Discussion	35
5	Conclusions and Future Work	37

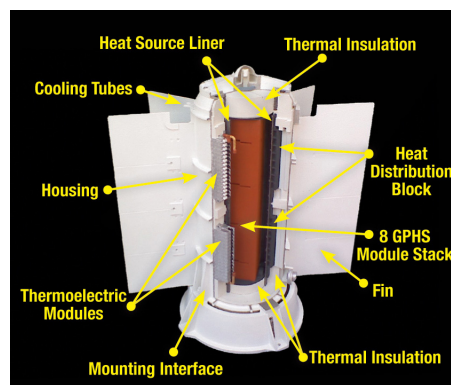
1 Introduction

The high rate of alpha decay of the plutonium-238 isotope lends the material to be used for many unique space applications where the reach of solar radiation is either too weak or unavailable. With a power density of 0.54 watts per gram, plutonium-238 has been used to power space exploration satellites from mars rovers to deep space probes. Los Alamos National Laboratory (LANL) has remained the primary location for fabrication of the plutonium oxide pellets. In an effort to apply modern techniques and tools towards supporting LANL's fabrication responsibilities, PUMA was created under an LDRD funded program to gain understanding of plutonium oxide heat source pellets during fabrication.

The radioactive nature of plutonium-238 inherently makes it difficult to produce, fabricate, and handle. Pu-238 is created during irradiation of U-235 in nuclear reactors, and is fabricated into oxide pellets (Fig. 1.1a). The pellets are in turn placed inside an iridium cladding and assembled into a Radioisotope Thermoelectric Generator (RTG) (Fig. 1.1b).



(a)



(b)

Figure 1.1: a) Pu-238 oxide pellet and b) one type of RTG assembly.

During fabrication of heat sources, a 20-30% failure rate is observed due to severe fragmentation and failure of the pellet. The fabrication involves hot-pressing PuO_2 powder in a graphite die, followed by sintering in an argon atmosphere. During the hot pressing stage, interactions between the oxide pellet and the graphite die results in reduction of the pellet to PuO_{2-x} and production of carbon monoxide. The final sintering step oxidizes the pellet back to stoichiometry. The reason for the cracking is unknown, and only limited measurements are available due to the extreme risk in working with Pu-238. As a result, a combination of simulation and surrogate work was funded as

a means to get a handle on the state of the pellet as it progresses through the different fabrication stages.

The proposed goal of gaining understanding of plutonia pellets by tangentially using simulation and surrogates (i.e. cerium oxide), instead of by direct interrogation, is motivated by several factors. First, the “non-hazardous” surrogate requirement necessarily means the material is not self heating. As a result, the temperature gradient that is produced in a typical Pu-238 pellet will be missing from any surrogate work, or will be fundamentally different if other means are used to heat the surrogate (e.g. electrical heating). The surrogate work allows for experimental techniques to be applied and assessed in a less risky environment, enabling a reduced set of experiments to be developed for eventual application to Pu-238. Finally, the inherent difficulty in working with non-stoichiometric oxide ceramics makes it difficult to accurately assess the stoichiometry of the material at high temperatures. Therefore, a combined approach can be developed that uses experiments at low temperatures with a stable stoichiometry and atomic scale simulations to estimate high temperature properties.

During fabrication, the plutonia pellet is first passed through a hot pressing stage, where PuO_2 powder is subjected to high temperature and external compression to form a solid pellet. Subsequently, the thermal expansion of the pellet compared to the graphite is such that the pellet will effectively pull away from the die as the pellet cools after pressing. As a result, the die is assumed here to only impart an insulating effect, with no physical interaction required to be captured during the simulation. After the pellet is pressed, it is removed from the graphite die and transferred to a high temperature furnace. Due to the specific activity of plutonium-238, the pellet retains a temperature gradient throughout fabrication and deployment, determined by the total heat generation and thermal conductivity of the pellet. Except for the initial hot pressing stages in which the die has not yet fully closed, the change in the temperature gradient is the driver for the stresses in the pellet via thermal expansion strain. Unlike the sintering of traditional materials where heat generation is absent, the thermal gradient imposed by the self heating results in a complex interaction between thermal expansion and the temperature gradient. Due to these complications, the pellet experiences a non-trivial stress state which is proportional to the deviation in the temperature gradient from the gradient experienced during pellet sintering.

Throughout the fabrication process, the major physical phenomenon, i.e. thermo-physical, chemical, and density changes, are all tightly coupled via the local temperature and stoichiometry. The tightly coupled physical behavior of the materials, complicated by the temperature gradient in the pellet and the difficulty presented by plutonium-238 handling, provides the clear motivation for simulations of the plutonia using advanced simulation methods and models.

2 PUMA Code Description

2.1 MOOSE

PUMA is built on top of the open source MOOSE framework [1], which essentially combines the C++ finite element library `libMesh` [2] with the nonlinear solver package `PETSc` [3] in a developer friendly package. MOOSE is organized into the basic coding framework which provides the fundamental computer science pieces, with much of the physics separated into “modules” (e.g. solid mechanics behavior, heat conduction). PUMA leverages much of the work already in MOOSE, with the addition of specific material properties, models, and physics required to simulate PuO_{2-x} and surrogates. As such, this document will focus on what has been implemented into PUMA, with only relevant details of the MOOSE package included where necessary.

MOOSE numerically solves a set of partial differential equations (PDE) using several different “objects”. For example, `Variables` retain the value of the quantity of interest, and are solved for using the physics implemented as `Kernels`. `Variables` are the traditional FEM solution set and are defined by the values solved for at quadrature points combined with the shape function associated with the variable. Supporting the calculation are `Materials`, which are calculated values defined at the quadrature points and utilized by the kernels. In addition, `AuxVariables` provide calculated values at the nodes and are defined by either nodal or elemental values and their associated shape function. Also present are `BCs` or boundary conditions, `Functions` or spatially independent mathematical formulations, and many other various objects that support MOOSE simulations.

The coding environment provided by MOOSE comes with a tradition of code development baked in to many of the tools in the MOOSE framework. This primarily exists in the form of verification tests that are implemented to verify the code runs as expected. This is especially important due to the relative infancy of MOOSE and some of the modules PUMA relies on. In the sections that follow, underlying verification tests have been created and included into the PUMA repository to ensure that the code is acting as expected. These tests span the relevant parametric space they are expected to operate in, and are individually related to hand calculations or python scripts to provide external confidence in the result. The reader is referred to the PUMA code repository for further details on the implemented tests.

2.2 PUMA objects

The code that exists within PUMA spans a small but essential subset of MOOSE objects, and can be summarized as:

- **Materials:** phase determination, thermal conductivity, specific heat, thermal expansion, and elasticity moduli, for PuO_2 , CeO_2 , and graphite;
- **AuxKernels:** stoichiometry calculations, thermal expansion zero-stress formulations, and matrix visualization tools;
- **Functions:** a ramp function that provides the necessary temperatures to a Dirichlet boundary condition to capture the fabrication steps.

2.2.1 Materials

The materials defined by PUMA consist of Young’s Modulus, λ , and Poisson’s ratio, ν , for the solid mechanics properties, thermal conductivity, λ , and specific heat, c_p , for the thermal properties. Also important is the coefficient of thermal expansion, $\Delta L/L_0$, the heat generation rate, \dot{Q} , for Pu-238, and phase information given the temperature and stoichiometry. Properties are implemented for ceria, plutonia, and graphite in varying degrees of complexity. In general, ceria models are the most mature (e.g. thermal conductivity), with plutonia models relying on the limited available values until more extensive data are available. Only the thermal properties for graphite are included since the graphite die only acts as an insulator in any PUMA simulations, and imparts no physical strength or influence.

CeriaElasticityTensor

The Young’s modulus and Poisson’s ratio for Ceria is based on nano-indentation measurements on CeO_2 [4]. Although there is tremendous discrepancies in the data, the values seem to be an adequate starting point;

$$\text{Young's Modulus, } E = 250.0 \text{ [MPa]} \quad (2.1)$$

$$\text{Poisson's ratio, } \nu = 0.31 \quad (2.2)$$

No dependence on stoichiometry or temperature is provided due to limited data, although it is expected that both the strength of the material should be eventually addressed.

CeriaPhase

For the temperatures and stoichiometries of interest, ceria exists as perfect fluorite CeO_2 crystal, defective fluorite CeO_{2-x} crystal, and the lower-symmetry $\text{Ce}_{11}\text{O}_{20}$ structure. The combinations of the phases leads to four general regions of interest listed in Table 2.1 encompassed by the bottom right corner of the phase diagram in Fig. 2.1.

The compositions of constituent fluorite phases in CeO_{2-x} have been implemented in PUMA by fitting elliptical functions to the miscibility curve in Fig. 2.1. The oxygen to metal ratio of the high O/M fluorite phase (RHS of the miscibility curve) is given by,

Table 2.1: Phase regions treated by CeriaPhase

Phases	Stoichiometry Span	Temperature span
$\text{Ce}_{11}\text{O}_{20}$, CeO_2	N/A	<452 K
$\text{Ce}_{11}\text{O}_{20}$, CeO_{2-x}	$x = 0 - 0.01$	452–723 K
CeO_{2-x} , CeO_{2-y}	$x = 0.07 - 0.14$, $y = 0.01 - 0.07$	723–964 K
CeO_{2-x}	outside miscibility gap	>964 K

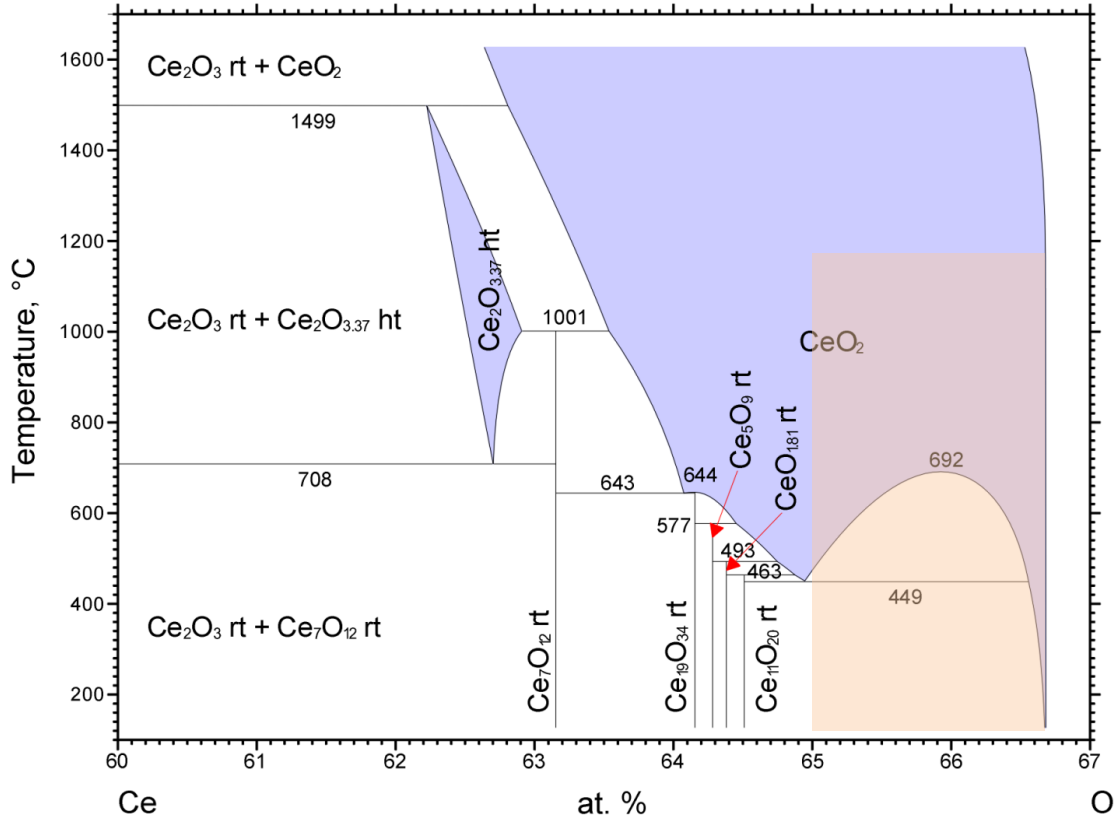


Figure 2.1: Ceria phase diagram [5]. The primary region of interest is in the orange box.

$$s_{F_1} = s_1 + (s_1 - s_0)^2 \sqrt{1 - (T - T_0)^2 / (T_1 - T_0)^2}, \quad (2.3)$$

$$\begin{aligned} s_{F_1} &= \text{stoichiometry (oxygen to metal atom ratio),} \\ T &= \text{temperature, [K],} \\ s_0 &= 2.00, \\ s_1 &= 1.93, \\ T_0 &= 451.88, [\text{K}], \\ T_1 &= 964.37, [\text{K}], \end{aligned}$$

where (s_0, T_0) represents the point on the phase diagram where the RHS of miscibility curve begins to deviate from perfect stoichiometry and (s_1, T_1) represents the peak in the miscibility curve. The function is designed such that at (s_0, T_0) and (s_1, T_1) the curve is parallel to the y-axis or x-axis in Fig. 2.1, respectively.

The oxygen to metal ratio of the low O/M fluorite phase (LHS of the miscibility curve) is given by,

$$s_{F_2} = s_0 - (s_1 - s_0)^2 \sqrt{1 - (T - T_1)^2 / (T_1 - T_0)^2}, \quad (2.4)$$

$$\begin{aligned} s_{F_2} &= \text{stoichiometry (oxygen to metal atom ratio),} \\ T &= \text{temperature, [K]} \\ s_0 &= 1.93, \\ s_1 &= 1.57, \\ T_0 &= 964.37, [\text{K}], \\ T_1 &= -8500, [\text{K}]. \end{aligned}$$

Here (s_0, T_0) represents the peak in the miscibility curve and (s_1, T_1) is an imaginary point outside of the phase diagram that captures the correct curvature of the LHS of the miscibility curve. The selection of elliptical functions that share an end coordinate (1.93, 964.37) ensures that the functions are continuous and smooth at the peak in the miscibility curve.

Given the oxygen concentration in each phase, the fraction of each phase in the multiphase regions are given by the lever rule. `CeriaPhase` provides phase information to other materials in order to consistently apply phase dependent properties. The so called phase “material property” contains the phase fraction, phase stoichiometry 2-x, and a flag to denote fluorite and non-fluorite phase structure.

CeriaThermal

`CeriaThermal` provides the thermal conductivity at a given quadrature point given a set of state variables of the system at that point. It achieves this first by defining the thermal conductivity of the individual phases, here CeO_{2-x} and $\text{Ce}_{11}\text{O}_{20}$. Given the information about the phase fraction, composition, and crystal structure of the constituent phases calculated by `CeriaPhase`, `CeriaThermal`

then calculates the effective thermal conductivity, which can then be used to solve the temperature distribution in the pellet.

The thermal conductivity for the defective and stoichiometric fluorite phase is defined by,

$$\kappa_{\text{CeO}_{2-x}} = \frac{1}{A_{\text{CeO}_2} + B_{\text{CeO}_2}T + C_{\text{CeO}_{2-x}}(2 - s_{F_i})} + \kappa_{\min}, \quad (2.5)$$

- $\kappa_{\text{CeO}_{2-x}}$ = thermal conductivity of CeO_{2-x} phase, [$\text{WK}^{-1}\text{m}^{-1}$],
- A_{CeO_2} = athermal phonon scattering of CeO_2 , [W^{-1}Km],
- B_{CeO_2} = phonon-phonon scattering of CeO_2 , [W^{-1}m],
- $C_{\text{CeO}_{2-x}}$ = oxygen vacancy phonon scattering in CeO_{2-x} , [W^{-1}Km],
- s_{F_i} = stoichiometry (oxygen to metal ratio) of CeO_{2-x} phase,
- κ_{\min} = minimum thermal conductivity of Ce-O system, [$\text{WK}^{-1}\text{m}^{-1}$].

A_{CeO_2} and B_{CeO_2} describe the thermal conductivity of the non-defective fluorite CeO_2 phase as a function of temperature. κ_{\min} is the minimum thermal conductivity of a Ce-O system, which is best determined from high T data. The inability of Ce^{4+} to be oxidized to Ce^{5+} means that maintaining stoichiometry is relatively simple by using an oxygen rich atmosphere, even to high temperatures. Therefore, by fitting Eq. (2.5) with $s = 2$ to the experimental data from Nelson et al. [6] up to 1723 K, $A_{\text{CeO}_2} = -0.005592 \text{ W}^{-1}\text{Km}$, $B_{\text{CeO}_2} = 0.0002650 \text{ W}^{-1}\text{m}$ and $\kappa_{\min} = 0.3208 \text{ W}^{-1}\text{Km}$ are defined.

The thermal conductivity of the non fluorite phase is defined by,

$$\kappa_{\text{Ce}_{11}\text{O}_{20}} = \frac{1}{A_{\text{Ce}_{11}\text{O}_{20}} + B_{\text{Ce}_{11}\text{O}_{20}}T} + \kappa_{\min}, \quad (2.6)$$

- $\kappa_{\text{Ce}_{11}\text{O}_{20}}$ = thermal conductivity of $\text{Ce}_{11}\text{O}_{20}$ phase, [$\text{WK}^{-1}\text{m}^{-1}$],
- $A_{\text{Ce}_{11}\text{O}_{20}}$ = athermal-phonon scattering of $\text{Ce}_{11}\text{O}_{20}$, [W^{-1}Km],
- $B_{\text{Ce}_{11}\text{O}_{20}}$ = phonon-phonon scattering of $\text{Ce}_{11}\text{O}_{20}$, [W^{-1}m],
- κ_{\min} = minimum thermal conductivity of Ce-O system, [$\text{WK}^{-1}\text{m}^{-1}$].

The control of the O/M of non-stoichiometric oxides as function of temperature provides a great challenge due to the sensitivity of O/M to the oxygen partial pressure. Furthermore, the initial O/M of a system may not be at thermal equilibrium with its environment and as the oxidation or reduction kinetics increase with temperature the O/M may begin to vary. LFA experiments carried out by LANL showed evidence that the hypo-stoichiometric CeO_{2-x} pellets began to oxidize at high temperature leading to a recovery in thermal conductivity, as phonon scattering oxygen vacancies were filled. Subsequently, oxidation experiments indicate that oxidation kinetics are sufficiently low below 623 K to provide confidence that the O/M is not significantly changed from the starting pellet. On that basis $A_{\text{Ce}_{11}\text{O}_{20}} = 0.1382 \text{ W}^{-1}\text{Km}$ and $B_{\text{Ce}_{11}\text{O}_{20}} = 0.0006198 \text{ W}^{-1}\text{m}$ were parameterized by fitting Eq. (2.8) to experimental measurements of the thermal conductivity of two-phase

CeO_{2-x} for $0 < x < 0.13$ and $300 \text{ K} < T < 623 \text{ K}$.

As can be seen in Fig. 2.1, below 623 K the defective fluorite phase (RHS of miscibility curve) is nominally stoichiometric and degradation due to total O/M change is primarily due to increase in the $\text{Ce}_{11}\text{O}_{20}$ phase fraction. Consequently, it is not possible to accurately parameterize the oxygen vacancy phonon scattering parameter $C_{\text{CeO}_{2-x}}$ using the available experimental data. Therefore, molecular dynamics (MD) simulations were carried out using the CRG potential [7] and the non-equilibrium method to investigate the change in thermal conductivity of the fluorite CeO_{2-x} lattice as a function of x by randomly distributing oxygen vacancies. The effect of the charge compensating Ce^{3+} defect (localized electron) was assumed to be negligible. By fitting Eq. (2.5) to the MD data $C_{\text{CeO}_{2-x}}^{\text{MD}} = 7.15 \text{ W}^{-1}\text{Km}$ was determined. This parameter results in too great a degradation in thermal conductivity compared to experimental data, even when considering that the high temperature experimental data is overestimating thermal conductivity due to reduction.

A potential source of error in the MD prediction of defect scattering is the poor description of electronic polarizability due to the use of rigid ion interatomic potentials [7]. Therefore, all polarizability around the charged defect is accommodated by ionic relaxation (strain) that, unlike electronic polarization, can scatter phonons. On the other hand, DFT techniques can capture the electronic polarization and give a more accurate description of the ionic strain around a defect. Therefore, the volumetric strain, ϵ_V , around an oxygen vacancy was calculated using density functional theory (DFT) and compared to the strain field around the defect in MD, finding $\frac{\epsilon_{V,\text{DFT}}}{\epsilon_{V,\text{MD}}} = 0.45$. This volumetric strain can be adjusted in relation to the cross-sectional area of the strain field that is experienced by phonons and then used to correct the MD determined oxygen vacancy phonon scattering parameter,

$$C_{\text{CeO}_{2-x}} = C_{\text{CeO}_{2-x}}^{\text{MD}} \left(\frac{\epsilon_{V,\text{DFT}}}{\epsilon_{V,\text{MD}}} \right)^{\frac{2}{3}}, \quad (2.7)$$

where $C_{\text{CeO}_{2-x}} = 4.2 \text{ W}^{-1}\text{Km}$ is the final parameter used in Eq. (2.5) within CeriaThermal.

Given the formulation of the phase specific thermal conductivities, the thermal conductivity of the multiphase system is defined as,

$$\kappa = X_{\text{Ce}_{11}\text{O}_{20}} \kappa_{\text{Ce}_{11}\text{O}_{20}} + X_{F_1} \kappa_{\text{CeO}_{2-x}} + X_{F_2} \kappa_{\text{CeO}_{2-x}}, \quad (2.8)$$

$$\begin{aligned} \kappa &= \text{thermal conductivity of multiphase } \text{CeO}_{2-x} \text{ system, } [\text{WK}^{-1}\text{m}^{-1}], \\ X_{\text{Ce}_{11}\text{O}_{20}} &= \text{phase fraction of } \text{Ce}_{11}\text{O}_{20}, \\ X_{F_1} &= \text{phase fraction of high O/M } \text{CeO}_{2-x} \text{ fluorite phase,} \\ X_{F_2} &= \text{phase fraction of low O/M } \text{CeO}_{2-x} \text{ fluorite phase,} \end{aligned}$$

The specific heat for ceria was implemented as [8],

$$c_p = 262 + 0.392T - 2.03 \cdot 10^{-4}T^2, \quad (2.9)$$

c_p = specific heat, [J/kg/K],
 T = temperature, [K].

Porosity in the pellet will result in an overall reduction in thermal conductivity, implemented in PUMA using the general form [8],

$$\lambda = \lambda_{solid} \left(1 - \frac{2.5p}{1-p} \right), \quad (2.10)$$

λ = thermal conductivity of the porous material, [W/m/K],
 λ_{solid} = thermal conductivity of the dense material, [W/m/K],
 p = porosity.

CeriaThermalExpansion

The mean coefficient of thermal expansion for multiphase CeO_{2-x} is a weighted average of the constituent phases,

$$\alpha = X_{\text{Ce}_{11}\text{O}_{20}} \alpha_{\text{Ce}_{11}\text{O}_{20}} + X_{F_1} \alpha_{\text{CeO}_2} + X_{F_2} \alpha_{\text{CeO}_2}, \quad (2.11)$$

α = mean coefficient of thermal expansion of multiphase CeO_{2-x} system, [K^{-1}],
 α_{CeO_2} = coefficient of thermal expansion of CeO_2 , [K^{-1}],
 $\alpha_{\text{Ce}_{11}\text{O}_{20}}$ = coefficient of thermal expansion of $\text{Ce}_{11}\text{O}_{20}$, [K^{-1}],
 $X_{\text{Ce}_{11}\text{O}_{20}}$ = phase fraction of $\text{Ce}_{11}\text{O}_{20}$,
 X_{F_1} = phase fraction of high O/M CeO_{2-x} fluorite phase,
 X_{F_2} = phase fraction of low O/M CeO_{2-x} fluorite phase,

The coefficient of thermal expansion of the fluorite CeO_2 constituent phase is taken from the recommended CINDAS formulations [9],

$$\alpha_{\text{CeO}_2} = \frac{-2.500 \cdot 10^{-3} + 7.480 \cdot 10^{-6}T + 3.765 \cdot 10^{-9}T^2 - 6.191 \cdot 10^{-13}T^3}{T - 293}, \quad (2.12)$$

α_{CeO_2} = coefficient of thermal expansion of CeO_2 , [K^{-1}],
 T = temperature [K].

Non-stoichiometry is assumed to have no effect on the coefficient of thermal expansion of the defective-fluorite CeO_{2-x} lattice.

While keeping α_{CeO_2} fixed, the coefficient of thermal expansion of $\text{Ce}_{11}\text{O}_{20}$ is derived by fitting Eq. (2.11) to experimental data for the CeO_2 – $\text{Ce}_{11}\text{O}_{20}$ two-phase regime below 623 K, giving,

$$\alpha_{\text{Ce}_{11}\text{O}_{20}} = \frac{-1.4276 \cdot 10^{-3} + 2.6952 \cdot 10^{-6}T + 7.8802 \cdot 10^{-9}T^2 - 1.5321 \cdot 10^{-13}T^3}{T - 293}, \quad (2.13)$$

$$\begin{aligned} \alpha_{\text{Ce}_{11}\text{O}_{20}} &= \text{coefficient of thermal expansion of } \text{Ce}_{11}\text{O}_{20}, [\text{K}^{-1}], \\ T &= \text{temperature, [K]}. \end{aligned}$$

CeriaPhaseSwelling

Volumetric swelling of multiphase CeO_{2-x} occurs as function of O/M through the positive defect volume of oxygen vacancies in the fluorite phases and the greater lattice volume per Ce atom of the $\text{Ce}_{11}\text{O}_{20}$ phase compared to CeO_2 . The total volumetric swelling strain relative to O/M= 2 is defined as,

$$\varepsilon_V = X_{\text{Ce}_{11}\text{O}_{20}}\varepsilon_{\text{Ce}_{11}\text{O}_{20}} + X_{F_1}\varepsilon_{\text{CeO}_{2-x}} + X_{F_2}\varepsilon_{\text{CeO}_{2-x}}, \quad (2.14)$$

$$\begin{aligned} \varepsilon_V &= \text{volumetric swelling strain of multiphase } \text{CeO}_{2-x}, \\ \varepsilon_{\text{Ce}_{11}\text{O}_{20}} &= \text{volumetric swelling strain due to } \text{CeO}_2 \rightarrow \text{Ce}_{11}\text{O}_{20}, \\ \varepsilon_{\text{CeO}_{2-x}} &= \text{volumetric swelling strain due to } \text{CeO}_2 \rightarrow \text{CeO}_{2-x}, \\ X_{\text{Ce}_{11}\text{O}_{20}} &= \text{phase fraction of } \text{Ce}_{11}\text{O}_{20}, \\ X_{F_1} &= \text{phase fraction of high O/M } \text{Ce}_{2-x} \text{ fluorite phase}, \\ X_{F_2} &= \text{phase fraction of low O/M } \text{Ce}_{2-x} \text{ fluorite phase}. \end{aligned}$$

The volumetric swelling of the fluorite CeO_{2-x} constituent phases is defined as,

$$\varepsilon_{\text{CeO}_{2-x}} = s \frac{\Delta V_{V_O}}{V_{\text{CeO}_2}}, \quad (2.15)$$

$$\begin{aligned} V_{\text{CeO}_2} &= \text{volume of one } \text{CeO}_2 \text{ formula unit, } [\text{\AA}^3], \\ \Delta V_{V_O} &= \text{volume change due to one oxygen vacancy, } [\text{\AA}^3], \\ s_{F_i} &= \text{stoichiometry (oxygen to metal ratio) of } \text{CeO}_{2-x} \text{ phase}, \end{aligned}$$

where $V_{\text{CeO}_2} = 39.526 \text{ \AA}^3$ and $\Delta V_{V_O} = 6.870 \text{ \AA}^3$ are calculated from DFT and s is calculated in CeriaPhase for both fluorite phases.

The volumetric swelling strain due to the formation of $\text{Ce}_{11}\text{O}_{20}$ is defined as,

Table 2.2: Phase regions treated by `PlutoniaPhase`

Phases	Stoichiometry Span	Temperature span
$\text{PuO}_{1.52}$, PuO_2	N/A	< 608 K
$\text{PuO}_{1.61+x}$, PuO_{2-y}	$x = 0 - 0.06$, $y = 0 - 0.025$	$608 - 903$ K
PuO_{2-x} , PuO_{2-y}	$x = 0.17 - 0.30$, $y = 0.025 - 0.17$	$903 - 943$ K
PuO_{2-x}	outside miscibility gap	> 943 K

$$\epsilon_{\text{Ce}_{11}\text{O}_{20}} = \frac{V_{\text{Ce}_{11}\text{O}_{20}}}{V_{\text{CeO}_2}} - 1.0, \quad (2.16)$$

$$\begin{aligned} V_{\text{CeO}_2} &= \text{volume of one CeO}_2 \text{ formula unit, } [\text{\AA}^3], \\ V_{\text{Ce}_{11}\text{O}_{20}} &= \text{volume of one Ce}_{11}\text{O}_{20} \text{ formula unit per Ce atom, } [\text{\AA}^3], \end{aligned}$$

where $V_{\text{CeO}_2} = 39.526 \text{ \AA}^3$ is calculated from DFT and $V_{\text{Ce}_{11}\text{O}_{20}} = 40.745 \text{ \AA}^3$ has been selected to reproduce the experimentally observed bump in volume due to the $\text{Ce}_{11}\text{O}_{20} + \text{CeO}_{2-x} \rightarrow \text{CeO}_{2-x} + \text{CeO}_{2-x}$ phase transition at 723 K.

PlutoniaElasticityTensor

The Young's modulus and Poisson's ratio for plutonia is from [10]:

$$\text{Young's Modulus, } E = 248.4 \text{ [MPa]} \quad (2.17)$$

$$\text{Poisson's ratio, } \nu = 0.28 \quad (2.18)$$

No dependence on stoichiometry or temperature is provided due to limited data, although it is expected that both the strength of the material should be eventually addressed.

PlutoniaPhase

For the temperatures and stoichiometries of interest, plutonia exists as perfect fluorite PuO_2 , defective fluorite PuO_{2-x} , the bcc phase $\text{PuO}_{1.52}$, and the bcc phase $\text{PuO}_{1.61-1.67}$. The combinations of the phases leads to four general regions of interest listed in Table 2.2 encompassed by the bottom right corner of the phase diagram in Fig. 2.2.

The composition of the $\text{PuO}_{1.52}$ bcc phase, s_{bcc_1} , is constant up to 608 K.

For $\text{PuO}_{1.61+x}$, the stoichiometry is anchored at 1.61 at 608 K and proceeds to increase linearly with temperature to $x = 0.06$ until 903 K, as follows,

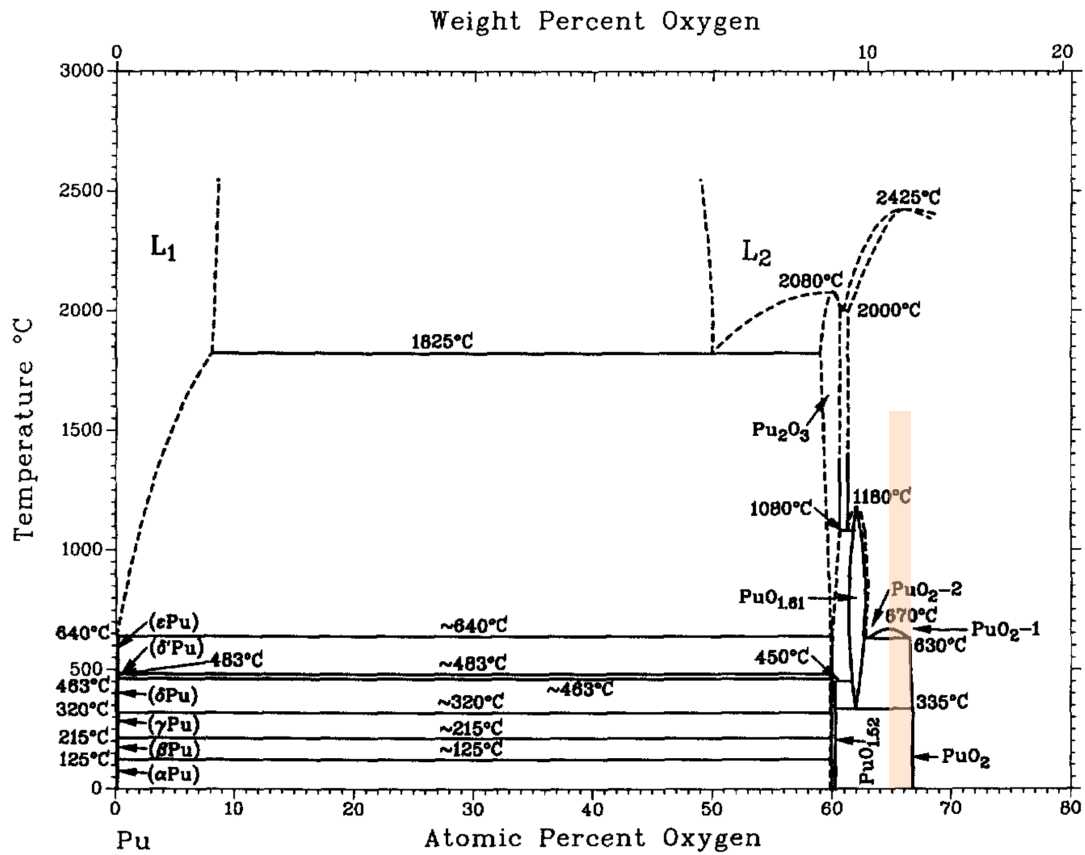


Figure 2.2: Plutonia phase diagram [11]. The primary region of interest is in the orange box.

$$s_{PuO_{bcc2}} = (0.000156)T + 1.531, \quad (2.19)$$

$$\begin{aligned} s_{PuO_{bcc2}} &= \text{stoichiometry of the PuO}_{1.61+x} \text{ phase, [W/m/K]}, \\ T &= \text{temperature, [K]}. \end{aligned}$$

The stoichiometry of high O/M fluorite phase (labelled PuO₂ – 1 in Fig. 2.2), s_{F_1} , is described by,

$$s_{F_1} = s_1 + (s_1 - s_0)^2 \sqrt{1 - (T - T_0)^2 / (T_1 - T_0)^2}, \quad (2.20)$$

$$\begin{aligned} s_{F_1} &= \text{stoichiometry (oxygen to metal atom ratio)}, \\ T &= \text{temperature, [K]}, \\ s_0 &= 2.00, \\ s_1 &= 1.83, \\ T_0 &= 827.69, [\text{K}], \\ T_1 &= 942.10, [\text{K}]. \end{aligned}$$

The composition of the low O/M fluorite phase (labelled PuO₂-2 in Fig. 2.2), s_{F_2} , is described by,

$$s_{F_2} = s_0 - (s_1 - s_0)^2 \sqrt{1 - (T - T_1)^2 / (T_1 - T_0)^2} \quad (2.21)$$

$$\begin{aligned} s_{F_2} &= \text{stoichiometry (oxygen to metal atom ratio)}, \\ T &= \text{temperature, [K]}, \\ s_0 &= 1.83, \\ s_1 &= 1.68, \\ T_0 &= 942.10, [\text{K}], \\ T_1 &= 873.95, [\text{K}]. \end{aligned}$$

Similarly to CeriaPhase, the selection of elliptical functions that share an end coordinate (1.83, 942.1) ensures that the miscibility curve is entirely continuous at the peak.

Given the oxygen concentration in each phase, the fraction of each phase in the multiphase regions are given by the lever rule.

PlutoniaThermal

Similar to the Ce₁₁O₂₀ phase, there is a lack of experimental data is available for the thermal conductivity of the PuO_{1.52} and PuO_{1.61} bcc phases. Furthermore, the crystal structure of these phases,

assumed here to be bcc, is not in full agreement throughout the literature, making atomic scale study of these phases highly challenging [11]. Therefore, it is assumed in PUMA that thermal conductivity of the non fluorite phases are the same as for a fluorite phase with the same composition, giving the multiphase thermal conductivity as,

$$\kappa = X_{bcc1} \kappa_{\text{PuO}_{2-x}} + X_{bcc2} \kappa_{\text{PuO}_{2-x}} + X_{F1} \kappa_{\text{PuO}_{2-x}} + X_{F2} \kappa_{\text{PuO}_{2-x}}, \quad (2.22)$$

$$\begin{aligned} \kappa &= \text{thermal conductivity of multiphase PuO}_{2-x} \text{ system, [WK}^{-1}\text{m}^{-1}\text{]}, \\ X_{bcc1} &= \text{phase fraction of PuO}_{1.52}, \\ X_{bcc2} &= \text{phase fraction of PuO}_{1.61}, \\ X_{F1} &= \text{phase fraction of high O/M PuO}_{2-x} \text{ fluorite phase,} \\ X_{F2} &= \text{phase fraction of low O/M PuO}_{2-x} \text{ fluorite phase,} \\ \kappa_{\text{PuO}_{2-x}} &= \text{thermal conductivity of PuO}_{2-x} \text{ fluorite phase, [WK}^{-1}\text{m}^{-1}\text{]}. \end{aligned}$$

The thermal conductivity of the defective-fluorite lattice is given by,

$$\kappa_{\text{PuO}_{2-x}} = \frac{1}{A_{\text{PuO}_{2-x}} + B_{\text{PuO}_{2-x}} T + C_{\text{CeO}_{2-x}} (2 - s_i)} + \kappa_{min}, \quad (2.23)$$

$$\begin{aligned} \kappa_{\text{PuO}_{2-x}} &= \text{thermal conductivity of PuO}_{2-x} \text{ phase, [WK}^{-1}\text{m}^{-1}\text{]}, \\ A_{\text{PuO}_2} &= \text{athermal phonon scattering of PuO}_2, [\text{W}^{-1}\text{Km}], \\ B_{\text{PuO}_2} &= \text{phonon-phonon scattering of PuO}_2, [\text{W}^{-1}\text{m}], \\ C_{\text{CeO}_{2-x}} &= \text{oxygen vacancy phonon scattering in CeO}_{2-x}, [\text{W}^{-1}\text{Km}], \\ s_i &= \text{stoichiometry (oxygen to metal ratio) of constituent phase,} \\ \kappa_{min} &= \text{minimum thermal conductivity system, [WK}^{-1}\text{m}^{-1}\text{]}, \end{aligned}$$

where $A_{\text{PuO}_2} = -0.02329 \text{ W}^{-1}\text{Km}$, $B_{\text{PuO}_2} = 0.0002333 \text{ W}^{-1}\text{m}$, and $\kappa_{min} = 0.3208 \text{ W}^{-1}\text{Km}$ were fitted to the experimental data from Cozzo et al. [12]. The strength of oxygen vacancy phonon scattering on the CeO_{2-x} lattice, $C_{\text{CeO}_{2-x}}$, is also used for PuO_{2-x} .

Equation (2.23) is used for all constituent phases in multiphase PuO_{2-x} , whereby the stoichiometry of each phase, s_i , is defined in `PlutoniaPhase`.

The specific heat for plutonia was implemented as [8],

$$c_p = 293.1 + 2.366 \cdot 10^{-3} T - 4.243 \cdot 10^{-6} T^2, \quad (2.24)$$

$$\begin{aligned} c_p &= \text{specific heat, [J/kg/K]}, \\ T &= \text{temperature, [K]}. \end{aligned}$$

The porosity equation implemented in Eq. (2.10) is applied in a similar fashion to the thermal conductivity of plutonia.

PlutoniaThermalExpansion

The coefficient of thermal expansion of multiphase PuO_{2-x} is taken as the recommended CINDAS formulation for stoichiometric PuO_2 [9],

$$\alpha = \frac{-2.030 \cdot 10^{-3} + 5.692 \cdot 10^{-6}T + 4.501 \cdot 10^{-9}T^2 - 1.031 \cdot 10^{-12}T^3}{T - 293}, \quad (2.25)$$

α = mean coefficient of thermal expansion of multiphase PuO_{2-x} , [K^{-1}],
 T = temperature, [K].

The O/M and phase dependence of thermal expansion are omitted, as is swelling due to O/M change.

GraphiteThermal

The thermal conductivity for graphite and can be calculated as a function of temperature as [8],

$$\lambda = 207.9 - 0.6098T + 9.767 \cdot 10^{-4}T^2 - 7.452 \cdot 10^{-7}T^3 + 2.127 \cdot 10^{-10}T^4, \quad (2.26)$$

λ = thermal conductivity, [W/m/K],
 T = temperature, [K].

The specific heat for graphite was taken from Butland and Maddison [13], and can be calculated as a function of temperature as,

$$c_p = (0.542 - 2.43 \cdot 10^{-6}T - 90.3T^{-1} - 4.34 \cdot 10^4T^{-2} + 1.59 \cdot 10^7T^{-3} - 1.44 \cdot 10^9T^{-4}) * 4184, \quad (2.27)$$

c_p = specific heat, [J/kg/K],
 T = temperature, [K].

GraphiteThermalExpansion

The mean coefficient of thermal expansion of graphite and can be calculated as a function of temperature as [8],

$$\alpha = 3.01 \cdot 10^{-6} + 3.85 \cdot 10^{-9}T - 1.32 \cdot 10^{-12}T^2, \quad (2.28)$$

α = mean coefficient of thermal expansion, [1/K],
 T = temperature, [K].

2.2.2 AuxKernels

MaterialMatrixAux

The phase material property defined in any Phase material retains the phase fraction and composition in a two-dimensional matrix. `MaterialMatrixAux` is an `AuxKernel` that extracts the value at the $\{i,j\}$ coordinates and sets an elemental `AuxVariable` which can then be used for outputting specific phase information either in the exodus file or in a `Postprocessor`.

StoichAux

In general, the diffusivity of oxygen in fluorite oxides is so rapid, it can be assumed to be infinite for the physics at hand. In addition, the stoichiometry gradient in the pellet due to thermodynamic conditions (e.g. temperature gradients) is currently assumed to be negligible, resulting in a constant pellet stoichiometry determined by the conditions at the surface of the pellet. In a general sense, this rate can be approximated by,

$$\frac{\partial s}{\partial t} = (s - s_{surf}^{eq}) \frac{A}{M} \exp\left(-\frac{Q}{k_b T_{surf}}\right), \quad (2.29)$$

- s = stoichiometry (oxygen to metal atom ratio),
- s_{surf}^{eq} = equilibrium stoichiometry at the pellet surface,
- A = pellet surface area, [m²],
- M = pellet mass, [kg],
- Q = reaction activation energy, [eV],
- k_B = Boltzmann constant, [eV/K],
- T_{surf} = average pellet surface temperature, [K].

`StoichAux` utilizes Eq. (2.29) to estimate the stoichiometry of the pellet, which is assumed constant throughout the pellet. s_{surf}^{eq} determines the limits of the reaction, and is set via a separate `AuxVariable` to mimic the reducing (i.e. $s_{surf}^{eq} \approx 1.88$ during hot pressing) and oxidizing (i.e. $s_{surf}^{eq} = 2.0$ during sintering) conditions observed during fabrication. The difference $(s - s_{surf}^{eq})$ ensures that the reaction rate slows as the equilibrium condition is reached, and prevents any over or undershooting of the stoichiometry, while the Q value determines the oxidation/reduction kinetics.

StressFreeTemperatureAux

In general, the stresses that develop in the PuO₂ pellet are due to changes in the temperature gradient introduced by the self heating characteristics of Pu-238. As the pellet experiences different temperatures in the fabrication steps, the change in the thermal conductivity modifies the temperature gradient, and in turn impacts the thermal strain, resulting in stresses in the pellet.

Thermal strains are calculated via the thermal expansion coefficient and the difference in temperature from a “stress-free” state. Internal thermal stresses are related to the thermal strain and the strength of the material. Thus as a strengthless powder, any free-swelling strain does not impart a stress. Only once the pellet is heated and pressed at high temperature, resulting reduction of porosity and bounding of the plutonia into a coherent shape, will accumulated strain result in internal pellet stress. As a result, the stress-free state and associated temperature is not set until some point during the hot pressing stage. All change in temperatures following a “freezing” of the stress-free state results in thermal strain and associated stresses.

In order to capture this numerically, `StressFreeTemperatureAux` was created to lock in the stress free temperature at some freeze in point,

$$T_{sf} = \begin{cases} T, & \text{for } t \leq t_{freeze}, \\ T_{sf}, & \text{otherwise,} \end{cases} \quad (2.30)$$

T_{sf} = stress free temperature, [K],
 T = temperature at the current time step, [K],
 t = time, [s],
 t_{freeze} = freeze time, [s].

Before the freeze time, Eq. (2.30) sets the stress free temperature to be the same temperature at the given time-step, ensuring that no strain is introduced by thermal expansion. After the freeze time, the stress free temperature is set at the temperature the pellet experienced at the freeze time. This means that for the remainder of the simulation, the stress state of the pellet is defined by the difference in the thermal gradient of the pellet at the t_{freeze} .

2.2.3 Functions

RampFunction

The stages of interest for modeling the behavior of the solid pellet are the initial hot pressing, and the high temperature sintering. In general, the information that defines each step is the ramp rates, hold temperatures, and hold times (Fig. 2.3). Also important is the coast time and coast temperature, which is the time it takes for the pellet to naturally cool to a known final temperature. `RampFunction` takes a list of ramp rates, hold temperatures, hold times, coast times, coast temperatures, and the desired minimum simulation steps between during the ramps and hold times, and provides the temperature of the outside of the hot press die, as well as time stepping information. Note, the temperature coasts are typically approximated as straight lines.

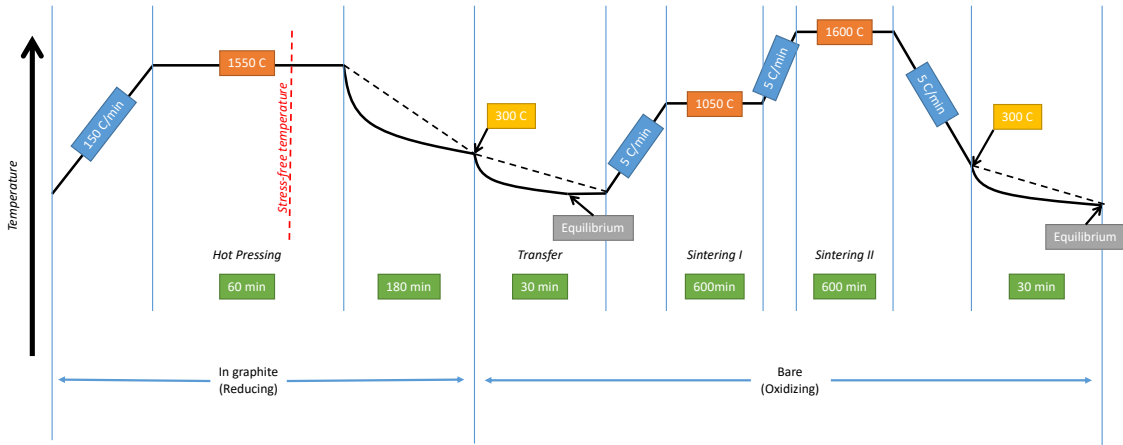


Figure 2.3: Example fabrication process including the hot pressing state and two high temperature sintering stages. The temperature ramps are in blue, the temperature holds are in orange, the hold and coast times are in green, and the coast temperature is in yellow. The coast times are typically approximated as linear and are designated by the dashed line.

2.3 Meshing

During the first stage of fabrication, the pellet is pressed in a graphite die assembly that creates the rounded right cylinder as pictured in Fig. 1.1a. After the first stage, the pellet is removed and sintered at high temperature in a bed of graphite. Temperatures for both stages are controlled through crude measurements such that the temperature information is limited to the die surface temperature in the first stage, and the furnace temperature set-point in the second stage. In order to capture the correct pellet temperature distribution during hot pressing, the entire die assembly is included to capture the insulating effect of the graphite.

The mesh for the pellet and die assembly is picture in Fig. 2.4a. Cylindrical symmetry about the centerline and reflective symmetry about the mid-plane of the pellet and die assembly can be exploited to simplify the problem.

A python script is included in the PUMA repository to handle the meshing of a bare pellet or pellet and die assembly. Also available is a dishing option to test various geometry types (Fig. 2.4b), similar to dishing of UO_2 pellets in commercial reactors.

2.4 Boundary Conditions

The boundary conditions required for the simulation of the pellet are the surface temperature of the graphite die assembly portrayed in Section 2.3, and the pinning of the mesh for the solid mechanics solve. Since the symmetry of the problem at hand typically allows a quarter mesh 2D-RZ to be

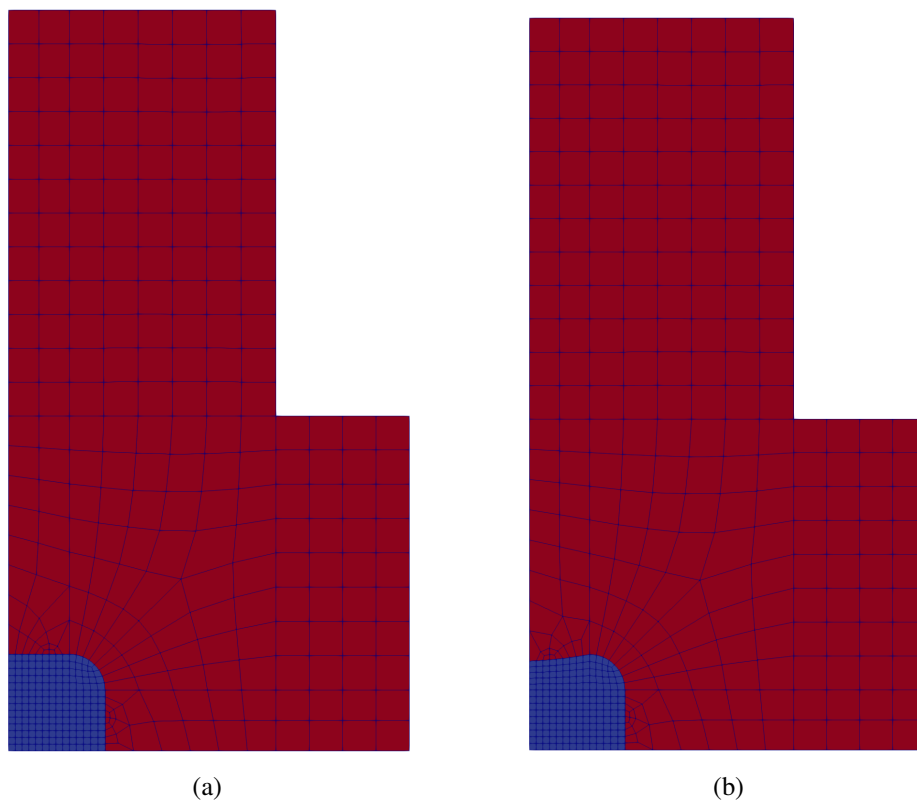


Figure 2.4: Mesh of pellet (blue) within the graphite die assembly red a) without and b) with pellet dishing.

utilized in PUMA simulations, the mesh is pinned in the x direction along the centerline of the pellet and graphite die, and pinned in the z direction along the bottom of pellet and graphite mesh.

During the first stage of fabrication, the temperature of the outside of the die is set using a `FunctionDirichletBC`, with the temperature given by the ramp defined in `RampFunction`. For the second high temperature sintering step, the temperature is set directly on the surface of the pellet.

2.5 Run Settings

The typical run settings used in PUMA simulations will be briefly listed here for informational purposes. The details of each setting can be found on the associated MOOSE documentation.

The relevant run settings are:

- `ReferenceResidualProblem` utilized for better convergence when solid mechanics is present;
- Second order, Lagrange elements;
- Finite strain formulation;
- Full SMP preconditioning;
- PJFNK solve option with a superlu preconditioner and line search turned off;
- `IterationAdaptiveDT` utilized to control the time-step based on the number of iterations required for convergence. `time-step_limiting_function` is linked to the `RampFunction` defined to ensure the time-step captures all temperature transitions and a minimum number of steps occur during each ramp and temperature hold;
- `sync_time` corresponding to the freeze time defined by `StressFreeTemperatureAux` used to ensure the simulation executes exactly at the freeze time.

3 Results

Using a mix of the new objects described in Section 2.2 and MOOSE objects, an example simulation of the fabrication process can be run to calculate the state variables of the pellet and behavior over time. What follows are results that vary important parameters such as thermal conductivity and thermal expansion compared to a baseline plutonia case. Unless listed otherwise, all cases use the example heating profile in Fig. 2.3, with material specific parameters listed in Table 3.1.

The primary focus of these simulations is to understand why cracking occurs in the pellets during fabrication. Since crack formation and propagation is difficult to simulate even for materials where all properties are known, the modeling efforts in PUMA have focused on the maximum principal stress as the primary indication for where or when cracking is most likely to occur. Using only the maximum principal stress as a failure metric ignores the impact of variations in the critical cracking stress or strain, which would provide the margin to cracking or failure. This is due to the difficulty in measuring the critical failure point of any material, along with the difficulty in working with PuO_2 or surrogates at high temperatures. In the results that follow, the take away should focus on the relative differences in the maximum principal strain and the impact of other state variables.

3.1 Plutonia baseline

The baseline plutonia case consists of the nominal heating profile with the best available material properties. Figure 2.2 plots the stoichiometry of the pellet as a function of time, as well as the heating profile for the hot-pressing and sintering stages. The parameters that control the stoichiometry changes (here $Q = 0.5$ eV, $s_{eq} = 1.88$ during hot pressing, $s_{eq} = 2$ during sintering) are fully empirical and are utilized to match the fact the pellet comes out of the hot pressing stage at $\text{PuO}_{1.88}$, and fully oxidizes back to PuO_2 during the sintering stage. The surface temperature, surface area, and mass of the pellet are automatically calculated for utilization in Eq. (2.29). Despite the simplistic formulation, the behavior of the pellet due to the stoichiometry changes can be analyzed to give a

Table 3.1: Run parameters by pellet material

Parameter	Plutonia value	Ceria value
Theoretical density [kg/m^3]	11500	7220
Porosity	0.15	0.15
Heat generation [W/cm^3]	3.64	0

qualitative assessment of how the stress changes over time.

The average thermal conductivity of the plutonia pellet ultimately drives the temperature gradient changes in the pellet, leading to thermal expansion driven strain and stress in the pellet. The change in the thermal conductivity during the fabrication process is provided in Fig. 3.2, and shows the strong temperature dependence in the thermal conductivity, as discussed in Section 2.2.1. For plutonia, the highest thermal conductivity occurs at the lowest temperatures. The stoichiometry changes in the pellet plotted in Fig. 3.1 also impact the thermal conductivity of the pellet. This is most clearly captured during the low temperature sintering stage, where the thermal conductivity increases due to oxidation of the pellet from $\text{PuO}_{1.88}$ back to PuO_2 .

The maximum, average, and minimum temperatures in the pellet are plotted in Fig. 3.3, and show the change in temperature over the fabrication cycles. The mesh defined in Section 2.3 includes the graphite die in order to capture the insulating effect of the die itself for the first hot-pressing cycle, while the boundary condition shifts to the outside of the pellet surface during the sintering operation. Figure 3.4 plots the difference between the pellet and die surface temperatures, and shows the insulating effect of the hot press only comes into play during the initial temperature ramp due to the specific heat of the pellet, resulting in a maximum deviation of 66 K. After the temperatures stabilize at the hot press hold temperature, the pellet surface is only one degree hotter than the surface of the die.

Also included in Fig. 3.4 is the temperature difference between the surface of the pellet and the maximum centerline temperature of the pellet. This difference tracks the change in the temperature gradient, which heavily impacts the stress state of the pellet, as will be discussed in the following sections. The temperature gradient is lowest at the lowest temperatures due to high thermal conductivity (Fig. 3.2).

The maximum principal stress of the baseline plutonia pellet is plotted in Fig. 3.5. At the location of highest maximum principal stresses, the pellet interior is in tension (hydrostatic stress > 0) and the pellet surface is in compression (hydrostatic stress < 0), as displayed in Fig. 3.6. Most interestingly, the location of highest stresses occur between the hot press and sintering stages, and at the end of the fabrication process. This can be explained by considering the temperature gradient in the pellet throughout the processing stages; during the initial ramp up of the hot pressing stage, the PuO_2 exists as a powder in an unclosed die assembly. As the temperature increases to the hot pressing hold temperature, sintering of the powder begins and the pellet begins to form into a solid structure. At this high temperature, the “stress-free temperature” is set via the techniques discussed in Section 2.2.2, delineated by the dotted line in Fig. 3.5. This essentially locks in the temperature gradient at which there is zero thermal stress in the pellet. Deviations from this gradient leads to a gradient in thermal strain, resulting in a correlated thermal stress. As a result, the highest maximum principal stress in Fig. 3.5 occurs at the lowest temperatures where the change in the temperature gradient relative to the stress-free state is the highest.

Complicating the stress profile during fabrication is the change in the stoichiometry; in general, the further from perfect stoichiometry PuO_2 deviates, the lower the thermal conductivity, as visible in Fig. 3.2 during the first and second temperature holds. As a result, the maximum principal stress increases at the lower temperature sintering step as the temperature gradient deviates further from

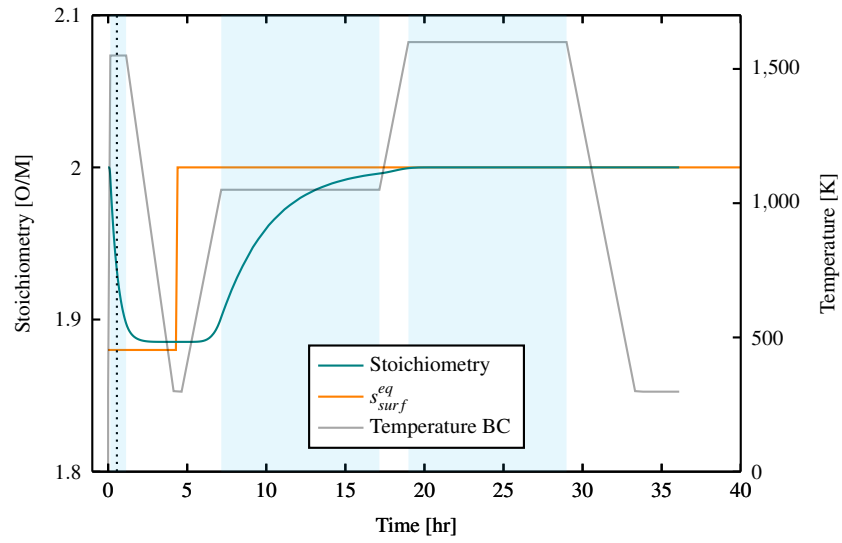


Figure 3.1: Stoichiometry for the plutonia baseline cases. The dotted line represents the time at which the stress free temperature is set, and the shaded blue regions correspond to the temperature hold times.

the gradient at stress-free temperature due to the increase in thermal conductivity.

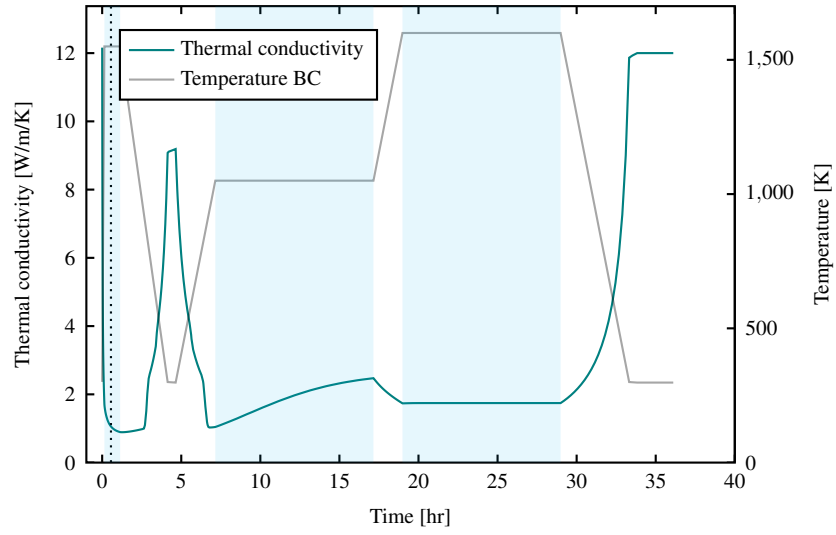


Figure 3.2: Average thermal conductivity for the plutonia baseline cases. The dotted line represents the time at which the stress free temperature is set, and the shaded blue regions correspond to the temperature hold times.

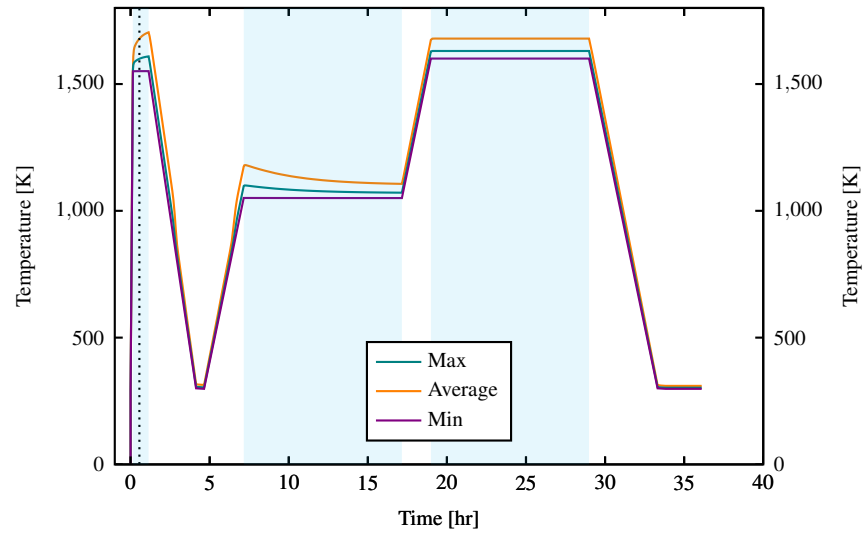


Figure 3.3: Temperatures for the plutonia baseline cases. The dotted line represents the time at which the stress free temperature is set, and the shaded blue regions correspond to the temperature hold times.

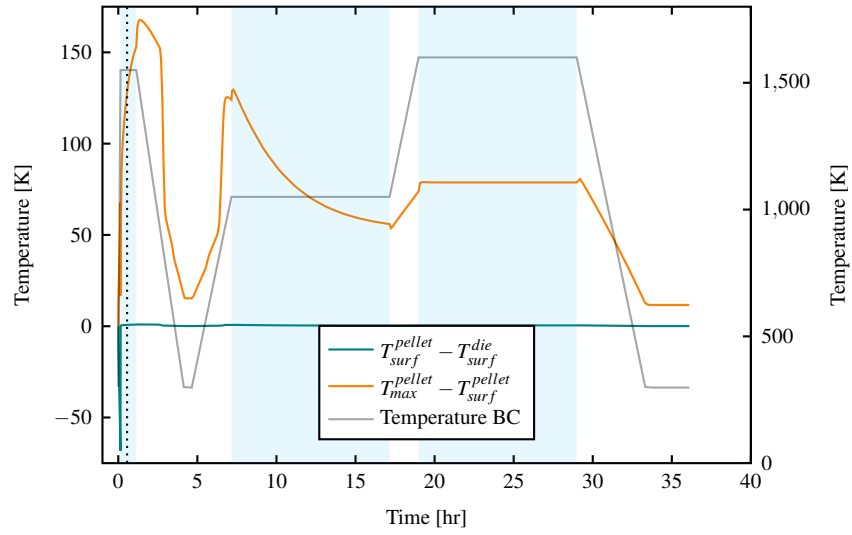


Figure 3.4: Difference between the minimum temperature and the boundary condition temperature, representing the difference in the temperature between the pellet surface and the graphite die surface. The dotted line represents the time at which the stress free temperature is set, and the shaded blue regions correspond to the temperature hold times.

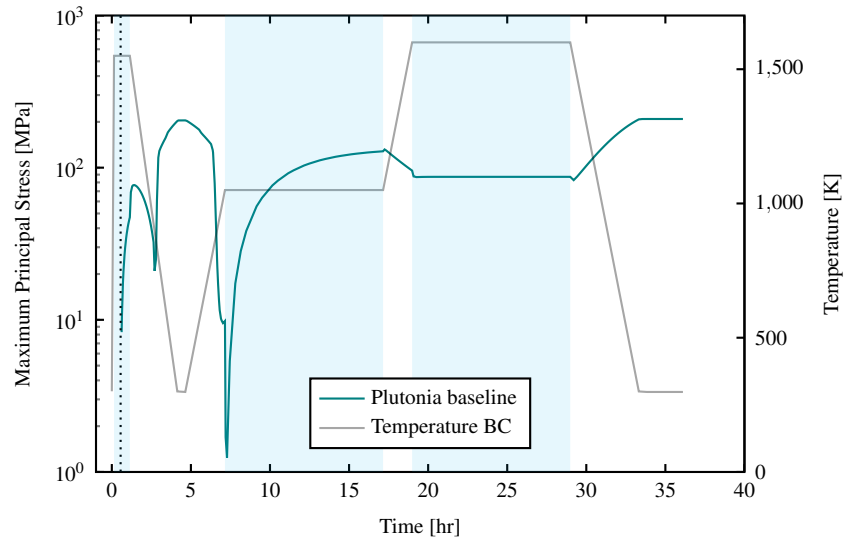


Figure 3.5: Maximum principal stresses for the plutonia baseline case. The dotted line represents the time at which the stress free temperature is set, and the shaded blue regions correspond to the temperature hold times. The maximum principal stress peaks around 5 hours at about 200 MPa, with the second highest peak at the end of the simulation around 100 MPa.

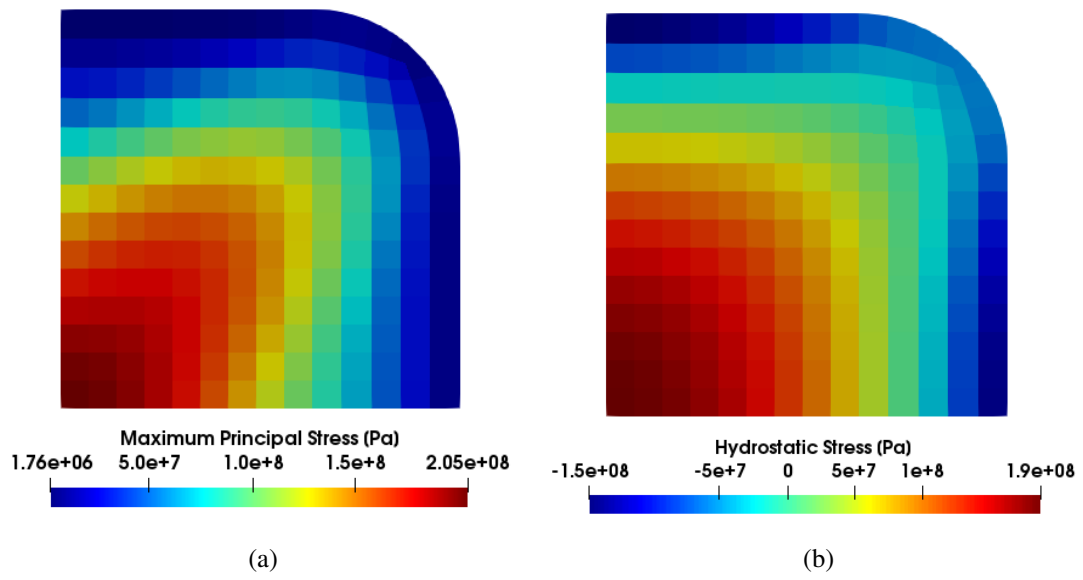


Figure 3.6: 2D slices of the plutonia pellet showing a) maximum principal stress and b) hydrostatic stress at the time of maximum stress between the hot pressing and sintering stages. Here, negative hydrostatic stress corresponds to a compressive stress.

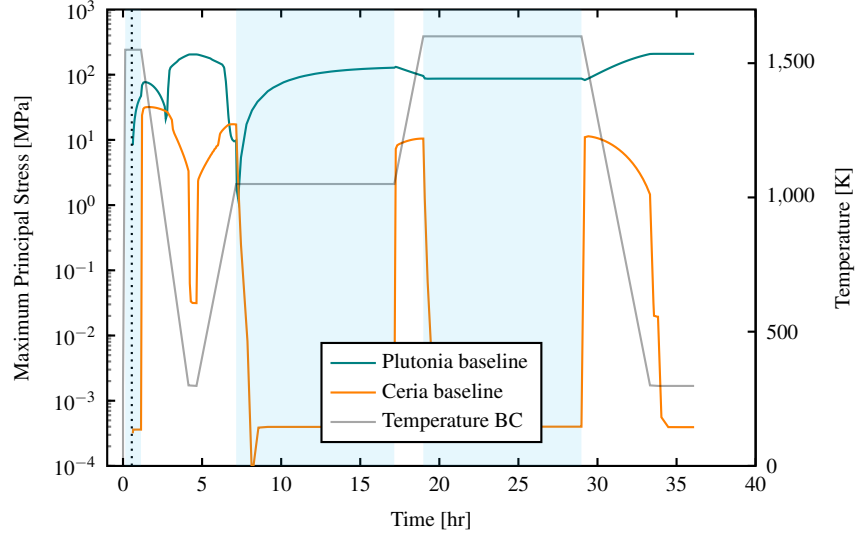


Figure 3.7: Maximum principal stresses for the plutonia and ceria baseline cases. The dotted line represents the time at which the stress free temperature is set, and the shaded blue regions correspond to the temperature hold times.

3.2 Ceria baseline

The ceria baseline case mimics the plutonia baseline case in many aspects including the same heating profile, surface reaction kinetics, and run parameters, while using material properties specific to ceria. Where the ceria baseline deviates most significantly is the absence of self-heating (Table 3.1), resulting in a flat temperature gradient throughout the pellet, except during temperature ramps. As a result, the locations of highest stress occur when temperature gradients exist in the pellet, i.e. during the temperature ramps, and are a direct result of a non-infinite specific heat. As the temperature gradient settles out in the pellet, the thermal expansion strain and stress gradients so too drop. This is in stark contrast to the maximum principal stress profile for plutonia where the highest stresses occurred at the lowest temperature holds.

The 2D stress profile for the ceria pellet at the point of highest stress i.e. during cooling in the hot pressing stage, is displayed in Fig. 3.8. Although the stress profile is from a different fabrication time than the plutonia stress profile in Fig. 3.6 due to different locations of maximum stress, it clearly shows that the stress profile is directly opposite of that for plutonia, with the surface in tension and the center in compression.

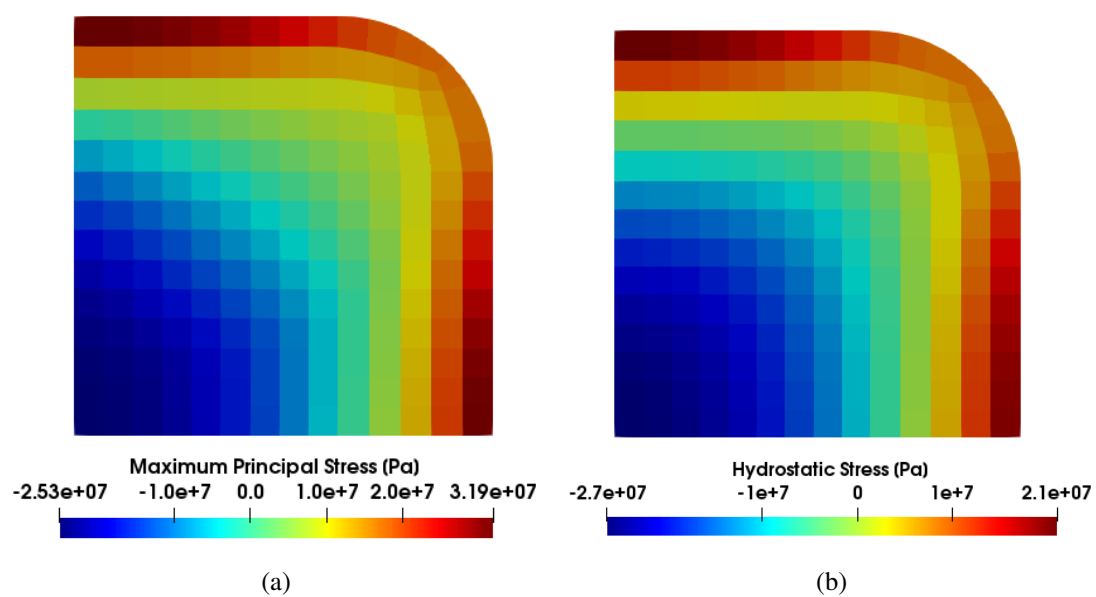


Figure 3.8: 2D slices of the ceria pellet showing a) maximum principal stress and b) hydrostatic stress at the time of maximum stress during the hot pressing stage.

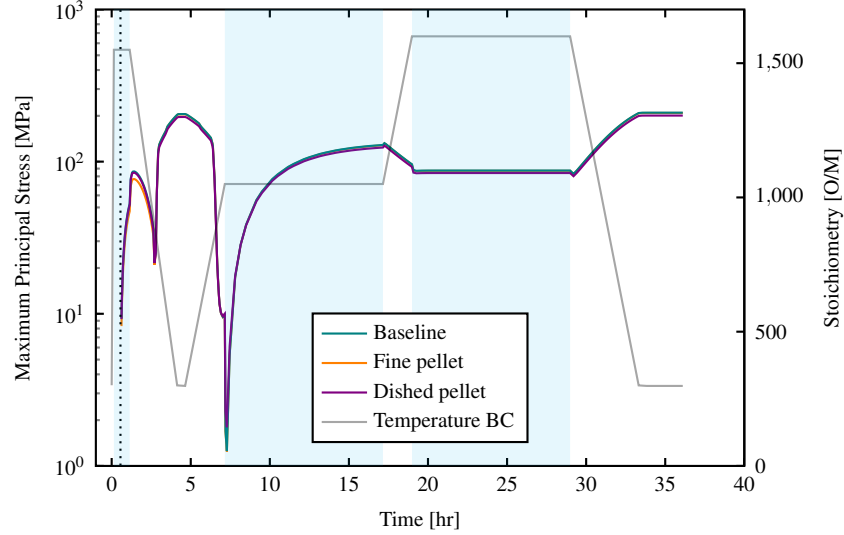


Figure 3.9: Maximum principal stresses for baseline plutonia, a dished pellet, and a refined mesh. The dotted line represents the time at which the stress free temperature is set, and the shaded blue regions correspond to the temperature hold times.

3.3 Mesh and Geometry changes

A simple mesh convergence check was performed to verify the mesh refinement was adequate enough to capture the maximum principal stress profiles. The mesh defined in Fig. 2.4a was refined significantly, resulting in a longer run time with no significant deviation in the calculated stress profile, as co-plotted in Fig. 3.9.

Also included in Fig. 3.9 is the maximum principal stress calculated for a dished pellet, as described in Section 2.3. Although the dished pellet sees success in UO_2 fuels, the stress profile experienced in the self-heating plutonia pellet remains insensitive to a dished profile.

3.4 Parametric studies

The difficulty in working with plutonia and ceria is well known, both from a logistical stand point due to human health hazards, but also due to difficulty in maintaining a fixed stoichiometry during property measurements. In an effort to assess the impact of the material properties on the maximum principal stress, a simple parametric study was performed for which the were thermal conductivity (Fig. 3.10), thermal expansion (Fig. 3.11), Young's modulus (Fig. 3.12), and heat generation (Fig. 3.13), were varied independently by $\times 2$ and $\times 0.5$. Surprisingly, the deviation in each parameter lead to similar increases and decreases in the maximum principal stress. Upon closer inspection, this behavior can be expected due to the direct coupling of the stress to the temperature gradient via boundary conditions and heat generation \rightarrow thermal conductivity \rightarrow thermal expansion strain \rightarrow stress. In general, halving the thermal conductivity, doubling the thermal expansion coefficient, doubling Young's modulus, or doubling the heat generation all lead to doubling the maximum principal stress.

The impact of the surface reaction rate was tested by either increasing or decreasing the overall surface reaction rate by a factor of two, resulting in the stoichiometry profiles plotted in Fig. 3.14. Clearly, the stoichiometry changes are very sensitive to the reaction rate, with a halved rate resulting in only minimal deviations in stoichiometry. The resulting stoichiometry changes lead to deviations in the maximum principal stress displayed in Fig. 3.15, with the slower reaction rate resulting in lower stress overall. This is primarily due to the fact that by limiting the change in thermal conductivity, the deviation in the temperature gradient can be reduced, resulting in less thermal strain overall. Doubling the reaction rate has only slight changes in the maximum principal stress since both temperature profiles generally reach the same stoichiometries by the end of the temperature holds.

In addition to deviations in the material property, the impact of the fabrication temperature profile was assessed for sensitivity to the maximum principal stress. The hold temperatures were increased and decreased by 100 K to assess their impact on the maximum principal stress. As displayed in Fig. 3.16, increasing the hold temperatures leads to a slight increase in the maximum principal stress due to a widening of the difference between the thermal gradient at the stress-free temperature and the thermal gradient at low temperature. The sensitivity to a rapid or slow temperature profile was also explored by either doubling or halving the ramp rates and hold times, resulting in maximum principal stress profiles as in Fig. 3.17. A slower ramp rate resulted in higher stresses in general due to the same processes that resulted in higher stress when a high reaction rate was utilized; due to the more rapid fabrication temperature profile, the pellet was unable to reach full equilibrium, resulting in a smaller deviation from PuO_2 , and less difference in temperature gradients throughout.

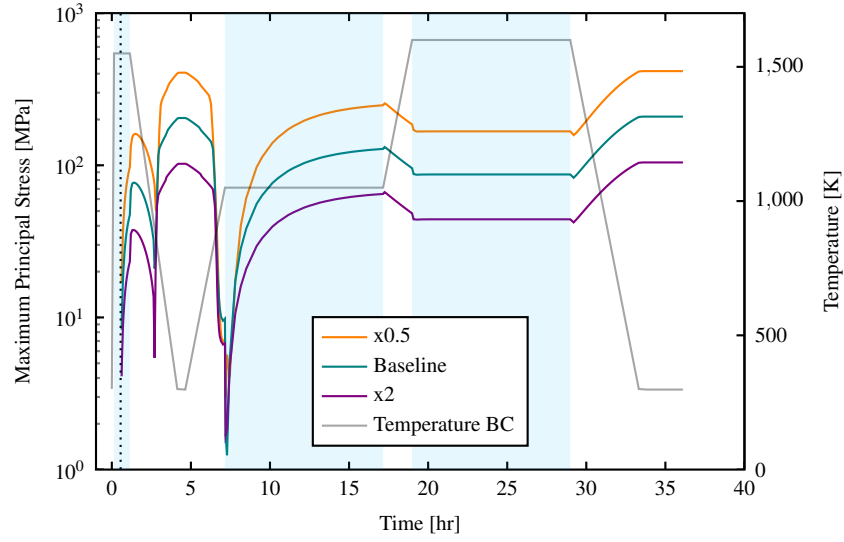


Figure 3.10: Maximum principal stresses for nominal, high, and low thermal conductivity. The dotted line represents the time at which the stress free temperature is set, and the shaded blue regions correspond to the temperature hold times.

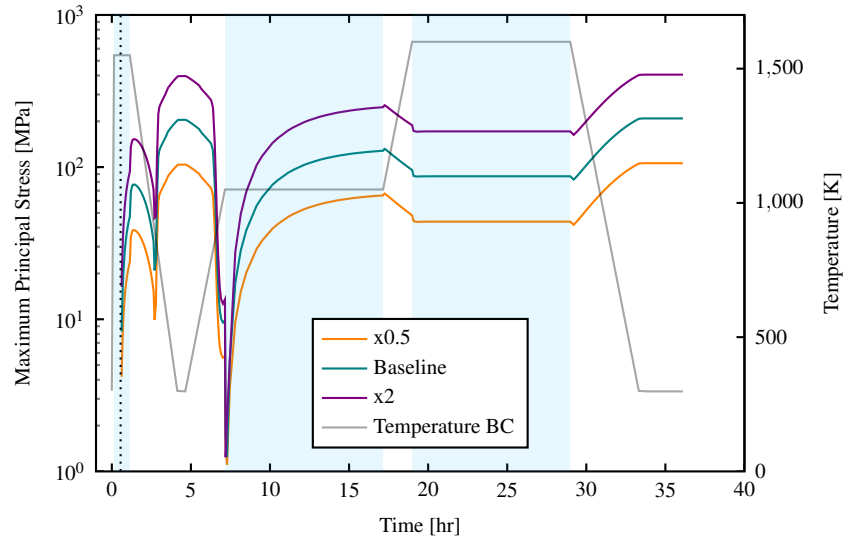


Figure 3.11: Maximum principal stresses for nominal, high, and low coefficient of thermal expansion. The dotted line represents the time at which the stress free temperature is set, and the shaded blue regions correspond to the temperature hold times.

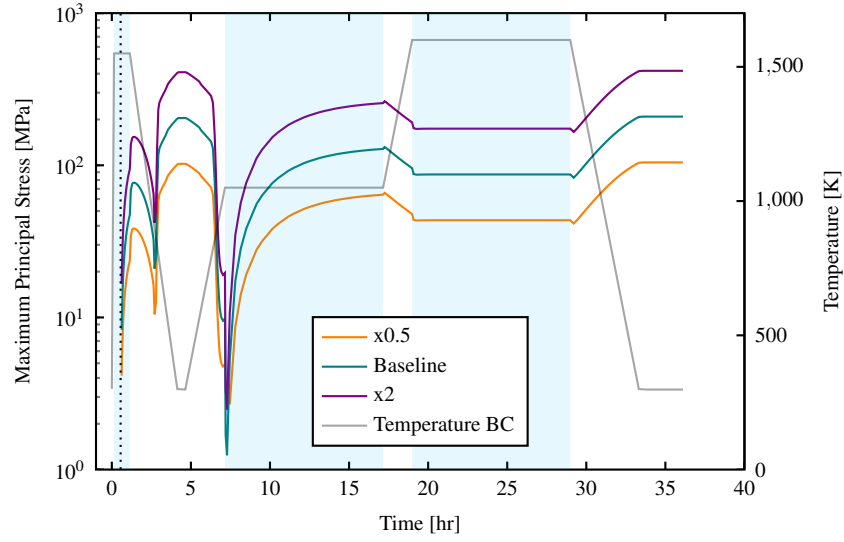


Figure 3.12: Maximum principal stresses for nominal, high, and low Young's modulus. The dotted line represents the time at which the stress free temperature is set, and the shaded blue regions correspond to the temperature hold times.

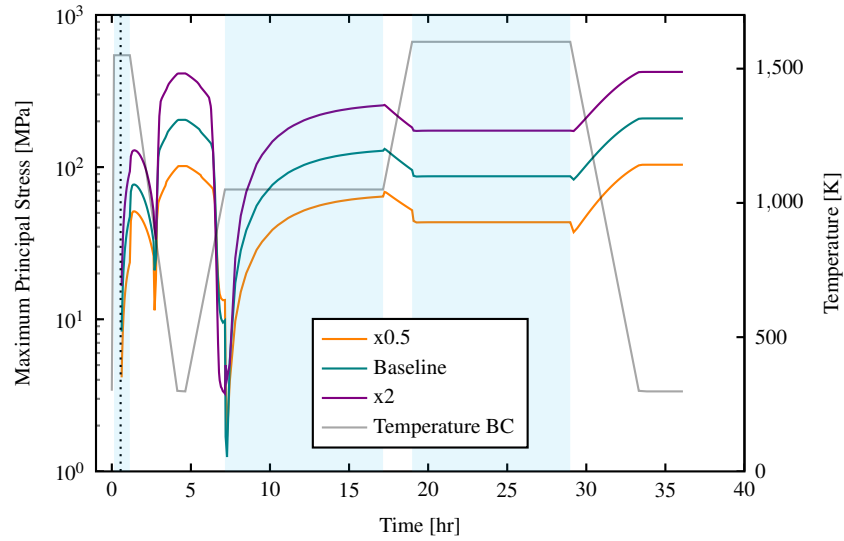


Figure 3.13: Maximum principal stresses for nominal, high, and low heat generation. The dotted line represents the time at which the stress free temperature is set, and the shaded blue regions correspond to the temperature hold times.

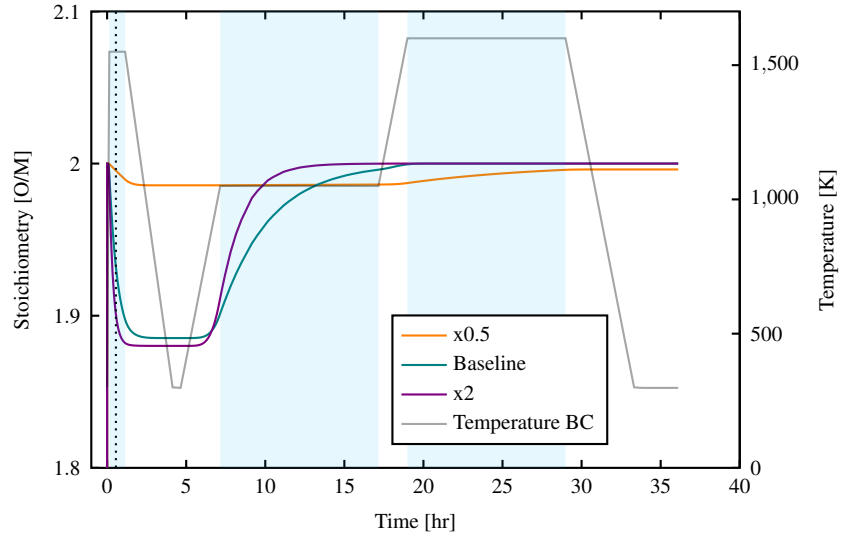


Figure 3.14: Stoichiometry for nominal, high, and surface reaction rates. The dotted line represents the time at which the stress free temperature is set, and the shaded blue regions correspond to the temperature hold times.

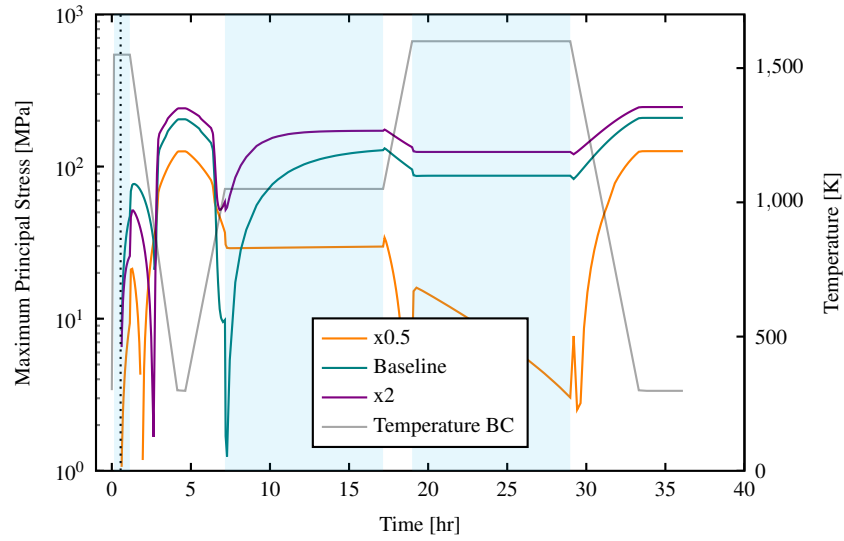


Figure 3.15: Maximum principal stresses for nominal, high, and surface reaction rate. The dotted line represents the time at which the stress free temperature is set, and the shaded blue regions correspond to the temperature hold times.

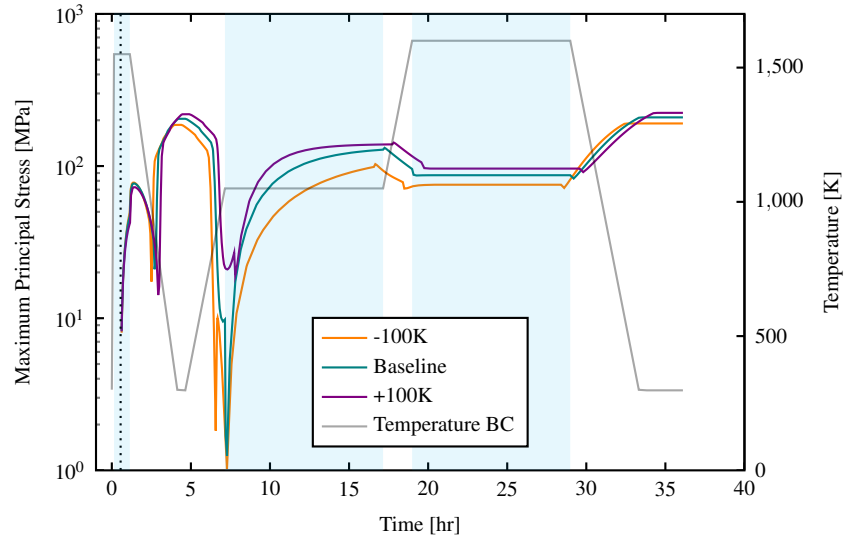


Figure 3.16: Maximum principal stresses for nominal, high, and low hold temperatures. The dotted line represents the time at which the stress free temperature is set, and the shaded blue regions correspond to the temperature hold times.

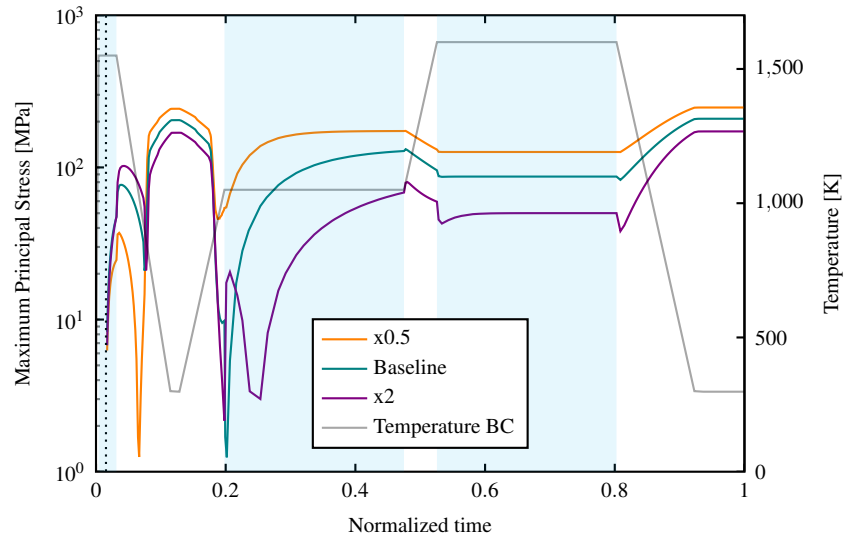


Figure 3.17: Maximum principal stresses for nominal, high, and low ramp rates with normalized time. The dotted line represents the time at which the stress free temperature is set, and the shaded blue regions correspond to the temperature hold times.

4 Discussion

The results presented in Section 3 represent a qualitative description of the behavior of plutonia during fabrication. It is important to note that the difficulty in working with both oxides at high temperature and with plutonium hinder the ability to capture material properties with a high level of confidence. As such, the simulations utilized a mix of newly measured surrogate properties, well vetted surrogate and plutonia properties, and wildly approximated definitions are utilized, as described in Section 2.2.1. In addition, the current state of PUMA does not capture all the physics occurring during fabrication such as sintering and stress relaxation. Regardless, general trends and conclusions can be made via comparisons to other materials such as ceria in Section 3.2, comparisons to differing pellet geometries as in Section 3.3, and simple parametric studies as in Section 3.4.

It is worth noting that the stress profiles in Section 3 present a conservative and qualitative over-estimate on the stresses within the pellet. The high temperatures that the pellet experiences will work to reduce some of the stresses the pellet experiences due to sintering and grain growth, ultimately driving down the extreme temperature stresses calculated at the end of the simulation. However, the pellet will likely never achieve a stress-free state due to the competing factors of high stress occurring primarily at the lower temperatures, reducing the driving forces for some of the stress-relaxing kinetics. This provides more confidence in the max principal stress peak between the hot pressing and sintering stages than the stress state during and after the sintering stages, resulting in the handling phase between the hot pressing and sintering stages as the point at which the pellet is most vulnerable.

The meshing studies in Section 3.3 indicate that the coarser mesh is adequate to capture the physics at hand. In addition, the finite element method allows for modifications in the mesh to be rapidly tested, as was shown with the dished pellet geometry. Unfortunately, the dished pellet showed little improvement in reducing the stress of the pellet.

The most valuable conclusion from the calculation in the maximum principal stress is that the point at which the pellet is most vulnerable is between the hot pressing and sintering stages. In general, the further away the temperature gradient in the pellet is away from the temperature gradient at the “stress-free temperature”, the higher the stresses will be in the pellet. This primarily occurs when the pellet is not in the die assembly or furnace and comes to an equilibrium temperature defined by the ambient temperature in the glove box. At the same time, it is in the glove box that the pellet is most handled, transferred, and manipulated. As discussed previously, the stress-state at the end of the fabrication is likely an over-estimate due to stress-relieving phenomena that are not currently captured. The high stress state and the high likelihood of a mechanical shock between the hot press and sintering stages indicates that the handling at this point may create the initial cracks

that likely lead to failure in the subsequent stages. By simply increasing the temperature of the pellet during these stages, the stress state of the pellet can be reduced, similar to walking up the temperature ramp in Fig. 3.5. For this, the self-heating nature of plutonium-238 can be exploited, with even simple insulation of the pellet likely resulting in a 100-200 K temperature increase that could reduce the stress-state of the pellet.

By exploring the impact of each material property to the maximum principal stress, the parametric study showed each parameter is almost equally important. This provides motivation to either more accurately measuring the properties themselves, or modifying the properties to ensure a more beneficial stress state. For example, the impact of the thermal conductivity is impacted by temperature as well as stoichiometry of the pellet. Through suppression of the surface reaction rate in which the plutonia becomes sub-stoichiometric during the hot press, it should be possible to reduce the high stress state that occurs between the hot pressing and sintering stages. This can be achieved by either changing the material of the die to a material other than graphite, or through incorporation of a liner that prevents reaction between the graphite and the oxide pellet.

Similar to modification of the die assembly to reduce reduction of the pellet, changing the fabrication temperature profile may also help reduce the stress state in the pellet. Although modifying the hold temperatures only has slight impact on the stress profile of the pellet, modifying the ramp rates and hold times results in differing stress profiles during fabrication. The rate of the temperature profile directly impacts the temperature gradients of the pellet, especially during heating of the ceria pellet, however this effect is suppressed in the self-heating plutonia pellet. Instead, the time at which the pellet is allowed to react with the graphite may reduce the stress of the pellet by preventing the pellet from deviating too far from perfect stoichiometry.

If a sintering model were to be implemented into PUMA, it may be possible to perform trade-off studies between the sintering and reduction phenomenon in the pellet. For example, a colder hot pressing temperature may result in the similar amount of sintering, but may reduce reduction of the pellet to a stoichiometry much closer to 2.0. This will be governed by the relative activation energies and further complicated by the coupling between physics (i.e. O/M dependence on sintering and surface area dependence on chemical kinetics). By running different fabrication profiles, the trade-offs between sintering and pellet stoichiometry can be analyzed with greater detail. This is especially attractive given the difficulty in working with plutonium-238, and may provide experimenters with insight into the most likely beneficial temperature profile before engaging in an experimental matrix.

5 Conclusions and Future Work

Plutonium-238 is an extremely valuable material, providing a unique solution for energy production where normal means are absent. The current failure rate of plutonia pellets during fabrication has and should continue to motivate LANL to better understand the behavior of the material during fabrication, and to develop tools to assess the state of the pellet without direct handling. PUMA was created to provide a tool to estimate the temperature, stress, and stoichiometry of the pellet during fabrication. By leveraging the existing MOOSE finite element framework, rapid development was achievable to capture the state variables of the pellet during the fabrication temperature profile.

By using the maximum principal stress an indicator for pellet failure, several conclusions can be drawn from PUMA simulations,

- PUMA can readily calculate the stoichiometry, temperature distribution, and stress profile of plutonia and ceria given any defined fabrication temperature profile;
- The insulating effect of the die assembly likely does not need to be included to capture the correct temperature distributions in the fuel;
- PUMA can readily assess different pellet shapes, but has shown that dishing of the top and bottom of the pellet does not effectively reduce the stress state of the pellet;
- The material properties that define the thermo-mechanical behavior of the pellet, i.e. thermal conductivity, thermal expansion, and Young's modulus, are all equally important;
- The reaction rate at the surface of the pellet during the hot pressing operation is important to capture, which has been shown to affect thermal conductivity here, but can be expected to affect thermal expansion and the material strength of the pellet as well;
- The highest stress state of the pellet occurs between the hot pressing and sintering stages, motivating further care to be exercised in handling the pellet during stage transfers;
- Increasing the temperature even slightly while in the glove box will help reduce the handling risk between stages;
- Incorporation of a sintering model into PUMA could allow for tradeoff studies between sintering and surface reaction, leading to an optimized fabrication temperature profile that achieves a similar end product with a reduced risk of pellet failure.

Although conclusions can be drawn using the simple material models currently implemented, PUMA will benefit from a host of future improvements. This includes better estimation of the fundamental material properties such as thermal conductivity, thermal expansion, and Young's modulus. Also, the simple surface reaction equation implemented via Section 2.2.2 needs to be expanded both to capture the relevant physics at hand such as the surface equilibrium conditions, as well as incorporation of experimentally derived reaction parameters. Beyond the material property requirements, the last major physical phenomenon missing from PUMA is the incorporation of a sintering model. This model can consist of simple master sintering curves, but may benefit from a more explicit treatment of the sintering and grain growth behavior in order to capture stress relaxation during the sintering stage of fabrication.

Acknowledgements

This work was sponsored by the Los Alamos National Laboratory Laboratory Directed Research and Development program. Los Alamos National Laboratory, an affirmative action/equal opportunity employer, is operated by Los Alamos National Security, LLC, for the National Nuclear Security Administration of the U.S. Department of Energy under Contract No. DE-AC52-06NA25396.

References

- [1] D. Gaston, C. Newman, G. Hansen, D. Lebrun-Grandié, MOOSE: A parallel computational framework for coupled systems of nonlinear equations, *Nuclear Engineering and Design* 239 (10) (2009) 1768–1778.
- [2] B. S. Kirk, J. W. Peterson, R. H. Stogner, G. F. Carey, libMesh: A C++ Library for Parallel Adaptive Mesh Refinement/Coarsening Simulations, *Engineering with Computers* 22 (3–4) (2006) 237–254, <https://doi.org/10.1007/s00366-006-0049-3>.
- [3] S. Balay, S. Abhyankar, M. F. Adams, J. Brown, P. Brune, K. Buschelman, L. Dalcin, A. Dener, V. Eijkhout, W. D. Gropp, D. Kaushik, M. G. Knepley, D. A. May, L. C. McInnes, R. T. Mills, T. Munson, K. Rupp, P. Sanan, B. F. Smith, S. Zampini, H. Zhang, H. Zhang, PETSc Web page (2018).
URL <http://www.mcs.anl.gov/petsc>
- [4] E. Wachtel, I. Lubomirsky, The elastic modulus of pure and doped ceria, *Scripta Materialia* 65 (2) (2011) 112–117.
- [5] H. J. Seifert, P. Nerikar, H. L. Lukas, Ce-O phase diagram, ASM Alloy Phase Diagrams Database, P. Villars, editor-in-chief; H. Okamoto and K. Cenzual, section editors; <http://www.asminternational.org>, ASM International, Materials Park, OH.
- [6] A. Nelson, D. Rittman, J. White, J. Dunwoody, M. Kato, K. McClellan, An Evaluation of the Thermophysical Properties of Stoichiometric CeO₂ in Comparison to UO₂ and PuO₂, *Journal of the American Ceramic Society* 97 (11) (2014) 3652–3659.
- [7] M. Cooper, M. Rushton, R. Grimes, A many-body potential approach to modelling the thermomechanical properties of actinide oxides, *Journal of Physics: Condensed Matter* 26 (10) (2014) 105401.
- [8] IAEA, Thermophysical Properties of Materials For Nuclear Engineering: A Tutorial and Collection of Data, Tech. Rep. IAEA-THPH, Vienna (2008).
- [9] CINDAS LLC, Recommended values from CINDAS. retrieved from CINDAS LLC thermophysical properties of matter database (tpmd). version 10.0 (2018).
URL <http://cindasdata.com>
- [10] V. Sobolev, Modelling thermal properties of actinide dioxide fuels, *Journal of Nuclear Materials* 344 (1-3) (2005) 198–205.

- [11] H. A. Wriedt, The O-Pu (oxygen-plutonium) system, *Bulletin of Alloy Phase Diagrams* 11 (2) (1990) 184–202.
- [12] C. Cozzo, D. Staicu, J. Somers, A. Fernandez, K. RJM, Thermal diffusivity and conductivity of thorium–plutonium mixed oxides, *Journal of Nuclear Materials* 416 (1-2) (2011) 135–141.
- [13] A. T. D. Butland, R. J. Maddison, The specific heat of graphite: An evaluation of measurements, *Journal of Nuclear Materials* 49 (1) (1973) 45–56.